Macromolecules
ARTICLE

Macromolecules **2009**, *42*, 8959–8968 **8959**
DOI: 10.1021/ma901754m

Evolution of Clay Morphology in Polypropylene/Montmorillonite Nanocomposites upon Equibiaxial Stretching: A Solid-State NMR and TEM Approach

Bo Xu, Johannes Leisen, and Haskell W. Beckham*

School of Polymer, Textile and Fiber Engineering, Georgia Institute of Technology, Atlanta, Georgia 30332-0295

Rund Abu-Zurayk, Eileen Harkin-Jones, and Tony McNally

Polymers Research Cluster, School of Mechanical and Aerospace Engineering, Queen's University Belfast, Belfast BT9 5AH, UK

Received August 5, 2009; Revised Manuscript Received August 24, 2009

ABSTRACT: Solid-state NMR and TEM were used to quantitatively examine the evolution of clay morphology upon equibiaxial stretching of polypropylene/montmorillonite (PP−MMT) nanocomposites up to a stretch ratio (λ = final length/initial length) of 3.5. ^{1}H spin−lattice relaxation times were measured by the saturation−recovery sequence. For the nanocomposites, initial portions of the magnetization recovery curves ($\leq\sim$20 ms) were found to depend on $\sqrt{t}$, indicative of diffusion-limited relaxation and in agreement with calculations based on estimates of the spin-diffusion barrier radius surrounding the paramagnetic centers in the clay, the electron−nucleus coupling constant, and the spin-diffusion coefficient. Initial slopes of these magnetization recovery curves directly correlated with the fraction of clay/polymer interface. New clay surface was exposed as a near linear function of strain. Long-time portions of the magnetization recovery curves yielded information on the average interparticle separations, which decreased slowly before reaching a plateau at $\lambda = \sim$2.5 as particles aligned. TEM images supported these findings and were used to define and quantify degrees of exfoliation and homogeneity from the NMR data. Exfoliation, defined as (platelets/stack)$^{-1}$, increased from 0.38 (unstretched) to 0.80 at λ = 3.5 for PP−MMT nanocomposites stretched at 150 °C and 16 s^{-1}. A lower stretch temperature, 145 °C, which is slightly below melting onset, led to an exfoliation degree of 0.87 at λ = 2.8, consistent with the ability of higher melt viscosities to allow for higher shear stress transfer. Exposure of new clay surface is attributed to aggregate breakup and orientation at low strains ($\lambda \leq \sim$2) and to platelets sliding apart at higher strains.

Introduction

Performance in polymer/clay nanocomposites (PCNs) depends on the nature of the interaction between polymer and clay and on details of the clay dispersion, which is affected by processing or deformation.[1−3] Relationships between processing conditions and clay morphology need to be firmly established to prepare PCNs with targeted properties. Some processing/structure and deformation/structure relationships have been reported for PCNs, mostly prepared by extrusion and injection molding[4−6] or deformed by uniaxial stretching.[2] On the other hand, little has appeared on the effect of multiaxial deformation of PCNs,[7,8] which is relevant for such processes as blow molding. A recent study of poly(ethylene terephthalate)/clay nanocomposites revealed how equibiaxial stretching aligned tactoids and increased exfoliation by sliding platelets apart.[9] Here we report on the evolution of clay morphology in polypropylene/montmorillonite nanocomposites that have been equibiaxially stretched. Mechanical properties have been reported for these materials[10] and will be connected with the quantitative descriptions of clay morphology presented below. We employed a combination of tools, but our analysis is based primarily on results from solid-state nuclear magnetic resonance (NMR) and transmission electron microscopy (TEM). The advantages and limitations of TEM and NMR, along with X-ray diffraction (XRD), have been well documented for characterizing clay dispersion in PCNs.[1,11−17] Here we use NMR and TEM in a complementary and integrated manner, for example, by defining some morphology descriptors that depend on both NMR and TEM data. The clay morphology as a function of strain is quantified and qualitatively correlated with the clay orientation.

PCNs containing homogeneously dispersed, completely exfoliated clay particles are rarely fabricated. For polyolefins, the production of such systems becomes increasingly difficult with high clay loadings, and the clay morphology is commonly characterized by a distribution of particle types and sizes including exfoliates, intercalates, and flocculated aggregates composed of two or more stacked platelets. This is certainly the case for polypropylene/clay nanocomposites,[5,18−22] the focus of the studies reported here. The clay that we used was montmorillonite (MMT), a naturally occurring layered silicate that contains small quantities of paramagnetic Fe^{3+} impurities. While these impurities do not affect most properties of nanocomposites containing MMT, they have a tremendous effect on the NMR relaxation characteristics, which is the basis of using NMR to characterize clay morphology.[12] The details and consequences of this paramagnetic effect are described in the following section.

*To whom correspondence should be addressed.

Published on Web 08/28/2009

Background

A. NMR Spin−Lattice Relaxation via Paramagnetic Centers. From the earliest days of NMR, it has been known that paramagnetic impurities in materials enhance spin−lattice relaxation.[23] Theoretical models that describe this enhanced relaxation were developed and tested, particularly on crystalline inorganic solids doped with known quantities of paramagnetic ions such as Cr^{3+}, Mn^{2+}, or Ce^{3+}.[23−29] Paramagnetic species enhance spin−lattice relaxation in two ways: (1) direct interaction with neighboring nuclei and (2) spin diffusion from remote nuclei to the paramagnetic centers. Thus, following a perturbation of the nuclear spin system (e.g., by placing a sample in a static magnetic field, or saturating it with rf pulses), the total rate at which the magnetization, M, changes with time, t, is

$$\left(\frac{\partial M}{\partial t}\right)_{\text{total}} = \left(\frac{\partial M}{\partial t}\right)_{\text{direct}} + \left(\frac{\partial M}{\partial t}\right)_{\text{diff}} + \left(\frac{\partial M}{\partial t}\right)_{\text{intrinsic}} \quad (1)$$

where $(\partial M/\partial t)_{\text{direct}}$ is the rate of magnetization change due to direct interaction with paramagnetic species, $(\partial M/\partial t)_{\text{diff}}$ is the rate of magnetization change resulting from spin diffusion to the paramagnetic relaxation sinks, and $(\partial M/\partial t)_{\text{intrinsic}}$ is the intrinsic rate of magnetization change due to interaction of the sample lattice with the static magnetic field (B_0). When relaxation intrinsic to the sample lattice is very slow, $(\partial M/\partial t)_{\text{intrinsic}}$ can be ignored.

The direct relaxation term has been given by

$$\left(\frac{\partial M}{\partial t}\right)_{\text{direct}} = \left(\frac{C}{r^6}\right)(M_0 - M) \quad (2)$$

where M_0 is the equilibrium magnetization, r is the distance from the paramagnetic center, and C is a constant describing the strength of the interaction between paramagnetic center and nucleus. After angular averaging, C can be expressed as

$$C = \frac{2}{5}S(S+1)\left(\gamma_p \gamma_n \hbar \frac{\mu_0}{4\pi}\right)^2 \frac{\tau_c}{1+\omega_n{}^2\tau_c{}^2} \quad (3)$$

where γ_p and γ_n are the magnetogyric ratios of the paramagnetic electron and observed nucleus, respectively, μ_0 is the magnetic constant ($4\pi \times 10^{-7}$ N/A^2), S is the spin number of the paramagnetic center (5/2 for Fe^{3+}), τ_c is the correlation time for the interaction of the paramagnetic center with the lattice, and ω_n is the Larmor frequency of the observed nucleus ($\gamma_n B_0$). As the distance from a paramagnetic center increases, nuclear relaxation due to direct interaction diminishes rapidly (note r^{-6} dependence in eq 2).

The spin-diffusion term in eq 1 has been given by $(\partial M/\partial t)_{\text{diff}} = D\nabla^2 M$, where D is the average spin-diffusion coefficient.[23] In the direct vicinity of paramagnetic centers, spin diffusion is suppressed due to the large local magnetic fields of unpaired electrons. For a surrounding spherical region with radius δ, the spin-diffusion coefficient is considered to be zero and δ is called the spin-diffusion barrier radius.[23−26,30] If the average distance between two paramagnetic centers (d_p) is much larger than the spin-diffusion barrier radius, and the direct relaxation rate is sufficiently high, the rate-limiting step in the overall relaxation is spin diffusion to the paramagnetic centers.[24,26,27] This is referred to as diffusion-limited relaxation and is characterized by magnetization growth following saturation that obeys a square-root-of-time dependence:

$$\frac{M(t)}{M_0} = \frac{4}{3}\pi^{3/2} C^{1/2} N_p t^{1/2} \quad (4)$$

where N_p is the number of paramagnetic centers per unit volume. Equation 4 holds in the following range of recovery times:[24,31]

$$\frac{\delta^6}{C} < t < C^{1/2} D^{-3/2} \quad (5)$$

Immediately following saturation of the spin system, no magnetization gradients exist in a sample. These gradients build up rapidly where relaxation by direct interaction with paramagnetic centers is most prevalent. As magnetization gradients develop, magnetization recovery is diffusion-limited and characterized by an initial square-root-of-time dependence for a finite time period defined by eq 5. Once gradients are established throughout the matrix, magnetization grows exponentially with time toward equilibrium:

$$\frac{M(t)}{M_0} = 1 - \exp(-t/T_1) \quad (6)$$

Since the transition from diffusion-limited to exponential magnetization growth is gradual, it could be beneficial to estimate the time limits of the diffusion-limited regime for a given sample according to eq 5.

B. Polymer−Clay Nanocomposites. Natural clays like montmorillonite contain paramagnetic impurities such as Fe^{3+} ions located within a central octahedral alumina layer sandwiched between two sheets of tetrahedral silica; the total thickness of this clay platelet is ~1 nm. When incorporated into a polymer to make a nanocomposite, these clays provide a source of enhanced NMR spin−lattice relaxation for the surrounding chain segments. In analogy to the paramagnetic impurities in crystalline compounds discussed above, the Fe^{3+} ions in the clay can shorten the T_1s of nuclei near the surface of the clay by direct interaction and of nuclei remote from the clay surface through spin diffusion. However, before analyzing data using the approach described above, some differences between inorganic crystals doped with paramagnetic impurities and polymer−clay nanocomposites (PCNs) should be considered. For example, in the doped inorganic crystals, the paramagnetic centers are homogeneously dispersed with typical concentrations (N_p) between 10 and 0.1 $\times$ 10^{19}/cm^3, which leads to average impurity separations, $d_p = 2 \times (3/4\pi N_p)^{1/3}$, between 2 nm and just over 12 nm, respectively.[28] In clays used for PCNs, the paramagnetic centers are present in similar and even slightly higher concentrations of 10^{19}−10^{21}/cm^3 (calculated from structural formulas and either density or unit-cell dimensions obtained from X-ray diffraction), but the clays are then dispersed, very often inhomogeneously, in polymeric matrices at concentrations typically of 1−5 wt %. The minimum separation between clay platelets can be estimated for an "idealized" nanocomposite (Δ_{ideal}), that is, one in which the clay is completely exfoliated and homogeneously dispersed:

$$\Delta_{\text{ideal}} = V_{\text{polymer}}/(V_{\text{clay}}/h_{\text{clay}}) \quad (7)$$

where V_{polymer} is the volume fraction of polymer, V_{clay} is the volume fraction of clay, and h_{clay} is the clay platelet height or thickness. Using densities of 0.91 and 2.6 g/cm^3 for polypropylene and montmorillonite, respectively, and h_{clay} = 1 nm, eq 7 was used to calculate interplatelet spacings

between 290 and 50 nm for 1−5 wt % clay, respectively. These dimensions would be even larger for clay aggregates that are not fully exfoliated. Thus, in PCNs, a greater majority of organic nuclei lie outside the spherical regions around the paramagnetic centers with radius d_p. Furthermore, the paramagnetic centers in PCNs are not in direct contact with the nuclei of the polymeric matrix but are embedded in the central layer of a three-layer platelet and therefore separated by a minimum of 0.5 nm from the nearest organic nuclei on the platelet surfaces. As the clay commonly exists as stacks of platelets, many of the paramagnetic centers can be even farther away from the nearest organic nuclei. A consequence of the very dilute nature of the paramagnetic centers in PCNs is that the intrinsic ^{1}H T_1s of the samples must be taken into account (see eq 1) as the T_1 differences between pure polymer and PCN may not be that great.

VanderHart et al. have discussed the influence of clay-embedded paramagnetic impurities on the NMR properties of polymers in PCNs[32−34] and showed how ^{1}H T_1 relaxation data can be used to quantify the degrees of exfoliation and dispersion homogeneity of the nanoscopic clay.[12] Working from a diffusion model that included both spin diffusion and longitudinal relaxation, they simulated the evolution of magnetization during a saturation−recovery experiment. Their model consisted of two regions: the bulk polymer and a thin layer (0.4 nm wide) near the clay surface that served as an interfacial relaxation sink. They simulated relaxation curves using finite element methods and representative T_1, D, and interplatelet spacing values (estimated using eq 7 for a well-exfoliated sample) for some polystyrene/montmorillonite nanocomposites. They then tried to approximate the calculated relaxation curves with a biexponential. The exponential fits very well for long recovery times but not so well for short times after saturation. The short-time behavior, specifically 5−50 ms, was better fit using a square-root-of-time dependence. Thus, their data are consistent with diffusion-limited relaxation. Most importantly, they described how the short-time portion of the recovery curves plotted versus $\sqrt{t}$ yielded straight lines with slopes that were directly proportional to the polymer−clay interfacial area, hence, amount of exfoliated clay. They used these initial slopes (S), corrected point-by-point for the intrinsic relaxation of the pure polymer, to calculate a degree of exfoliation, f. For a given clay and clay concentration

$$f = (\text{platelets/stack})^{-1} = S/[S_{\text{ref}}(\text{platelets/stack})_{\text{ref}}] \quad (8)$$

where S is the corrected initial slope for the sample and S_{ref} is the corrected initial slope for a reference material. Using a reference material known from TEM to be very well exfoliated, $(\text{platelets/stack})_{\text{ref}} = 1$ and the degree of exfoliation is simply calculated as a ratio of slopes. Furthermore, they also noted that the overall relaxation curves, approximately the exponential long-time portion of the magnetization recovery curves, yielded relaxation rates related to the quality of the clay dispersion.[32,34] They defined an overall paramagnetic contribution to the spin−lattice relaxation rate ($1/T_{1,\text{para}}$), which could be calculated simply by subtracting the rate due to the pure polymer ($1/T_{1,\text{polymer}}$) from the measured rate for the PCN ($1/T_{1,\text{PCN}}$):

$$\frac{1}{T_{1,\text{para}}} = \frac{1}{T_{1,\text{PCN}}} - \frac{1}{T_{1,\text{polymer}}} \quad (9)$$

While $1/T_{1,\text{para}}$ provides a relative measure of the homogeneity of the average interparticle separation, they also introduced a more quantitative measure. They calculated apparent interplatelet separations (Δ_{app}) using their model by matching the T_1s from the long-time portion of the magnetization recovery curves with experimental values. This apparent average separation was then compared to an "ideal" interplatelet spacing (Δ_{ideal} from eq 7) scaled by the degree of exfoliation (f from eq 8) to yield a quantitative measure of the homogeneity, ε:[12]

$$\varepsilon = (\Delta_{\text{ideal}}/f)/\Delta_{\text{app}} \quad (10)$$

where $\varepsilon = 1$ characterizes a sample with good homogeneity.

Experimental Details

Materials. Organically modified montmorillonite (MMT) was obtained from Southern Clay Products as their commercial product Cloisite 15A. Organically modified fluorohectorite (FH) was obtained from UniCO-OP Chemicals Japan as Somasif MAE. Samples were dried under vacuum at 110 °C for 48 h and cooled for 72 h at room temperature before all measurements. Structural characteristics of both clays are detailed in Table 1.

The polypropylene−montmorillonite nanocomposite was fabricated by melt compounding 5 wt % Cloisite 15A and isotactic polypropylene (PP, M_w = 250 kg/mol, M_w/M_n = 4.1) blended with 3 wt % PP-*g*-maleic anhydride (DuPont, Fusabond P, denoted as PP−MA). A PP/PP−MA blend without clay was also prepared using the same procedures as that used for the nanocomposite. In the following, the polymeric matrix is simply referred to as "polypropylene" or "PP" and the nanocomposite is referred to as "PP−MMT".

The PP and PP−MMT were compression-molded at 190 °C to form sheets with a thickness of 1 mm. This was followed by equibiaxial stretching in a home-built apparatus[41] for both PP and nanocomposite sheets. A series of samples with stretch ratios (λ = final length/initial length) of 1.5−3.5 were prepared by stretching at 150 °C (~5 °C below the peak melt temperature) with a strain rate of 16 s^{-1}. Some samples were also prepared at 145 °C (16 s^{-1}) and with a strain rate of 32 s^{-1} (150 °C). Prior to stretching, samples were held at their respective deformation temperature for 3 min.

Measurements. Solid-state NMR measurements were performed using a Bruker DSX-300 NMR spectrometer operating

Table 1. Structural Characteristics of Organically Modified Clays[a]

	montmorillonite (MMT)	fluorohectorite (FH)
mean formula unit[b]	$Na_{0.65}[Al,Fe]_4Si_8O_{20}(OH)_4$	$Na_{0.66}Mg_{2.68}(Si_{3.98}Al_{0.02})O_{10.02}F_{1.96}$
Fe_2O_3 content (wt %)	2.83[c]	0
CEC (mequiv/100 g)[d]	125	85−120
weight loss on ignition (%)	43	42
basal spacing (nm)	3.2	3.4
organic modifier[e]	2C18	2C18
area per cation (nm^2)[f]	~1.51	~1.35
T_1^H (ms)[g]	10	300

[a] Unless stated otherwise, information on MMT was obtained from technical literature provided by Southern Clay Products, Inc., while information on FH was taken from McNally et al.[35] [b] Taken from Xie et al.[36] for MMT and from Yang et al.[37] for FH. [c] This value from Southern Clay Products was determined by elemental analysis and corresponds to 4.96 wt % Fe_2O_3 or 3.47 wt % Fe in the pure clay (assuming all Fe^{3+}). [d] Cation exchange capacity; value depends on layer and edge charges; range for FH taken from Yang et al.[37] and Schmidt et al.[38] [e] Tallow-sourced dimethyldialkylammonium chlorides in which the alkyl tails consist of ~65 wt % C_{18}, ~30 wt % C_{16}, and ~5 wt % C_{14} for MMT and ~25 wt % C_{18}, ~74 wt % C_{16}, and ~1 wt % other for FH. [f] For FH, calculated from average layer charge of 0.33 mol per half unit cell (Si_4O_{10})[37] using method similar to Osman et al.;[39] for MMT, calculated beginning from typical surface area of ~750 m^2/g.[40] [g] Measured using saturation recovery.

at 7.05 T and a double-resonance CP/MAS probe. The organically modified clays were packed as powders into 7 mm (outside diameter) ceramic rotors for magic-angle spinning (MAS). Solid-state ^{13}C NMR spectra (10K scans) were measured using ^{13}C single-pulse excitation with ^{1}H high-power decoupling during detection. A recycle delay of 4 s, sample spinning speed of 5 kHz, and 90° pulse durations of 5 μs were employed.

For the polymer and nanocomposites, circles with diameters of ~6.8 mm were punched from the sheets using a leather hole punch and stacked into the 7 mm MAS rotors. All spin−lattice (T_1) relaxation experiments were conducted using the CP/MAS probe but on static samples without MAS. A saturation−recovery sequence was employed for recording the ^{1}H T_1 data.[12] For a given sample, 64 different relaxation delays from 0.5 ms to 10 s were measured with 16 averages each. The resulting ^{1}H spectra contained single peaks that were integrated to yield $M(t)$, where t is the respective delay time. Background signal was measured using an empty rotor and subtracted from each spectrum. Equilibrium magnetization (M_0) was obtained as the average integrated intensity from the spectra for t = 7, 8, 9, and 10 s (which are $>5T_1$). Plots of $M(t)/M_0$ vs t yielded the saturation−recovery curves. The overall ^{1}H T_1 was obtained by fitting to eq 6.

Because of lower signal-to-noise ratios for spectra at short recovery delays, the initial portions of the magnetization recovery curves (up to 50 ms) were measured using 64 scans for 32 separate relaxation delays. As described above, the resulting ^{1}H spectra were integrated to yield $M(t)$ and normalized by M_0. The normalized magnetization, $M(t)/M_0$, for the nanocomposites was corrected by subtracting point-by-point the $M(t)/M_0$ for the identically deformed pure polymer which was then plotted versus $\sqrt{t}$. The resulting initial magnetization build-up curves were fitted by linear regression.

High-resolution TEM images were recorded on a Phillips CM100 instrument using an accelerating voltage of 100 kV on ultrathin samples (typically 60 nm). For each stretching condition a total of 5−7 representative images were analyzed manually with respect to the average particle density, length, thickness, and separation using the software package ImageJ version 1.24o (NIH). All particles, including platelets, intercalates, and aggregates, were sampled.

Wide-angle X-ray diffraction patterns were recorded on a PANalytical X′Pert Pro diffractometer using Cu Kα_1 radiation generated at 45 kV and 40 mA (wavelength = 1.5406 Å). Samples were scanned at 0.02°/s in the range of 2θ = 1°−15°. The d_{001} basal spacing was calculated using the Bragg equation.

Differential scanning calorimetry (DSC) measurements were performed on a Seiko 220C at a heating rate of 10 °C/min to 200 °C. Thermogravimetric analysis (TGA) was conducted on a Seiko TG/DTA 320 in N_2. Samples were heated at 15 °C/min to 600 °C and held there for 10 min. Following this heat treatment, residual mass was taken as the pure clay content.

Results and Discussion

Solid-state ^{1}H NMR spin−lattice relaxation data were collected using the saturation recovery method for all PP and PP−MMT samples. Representative data are shown in Figure 1 for the PP−MMT and corresponding PP biaxially stretched to λ = 2.5. Solid-state ^{1}H NMR spectra (Figure 1a) were integrated and plotted versus recovery time to yield relaxation curves (Figure 1b) that are fit well with exponentials (eq 6) to yield single T_1s. While it is straightforward to observe that the relaxation rate for the nanocomposite is greater, it would be easy to overlook information that can be gleaned from the very initial portions of these recovery curves. Bourbigot et al. have shown the initial slopes of magnetization recovery curves are proportional to the clay−polymer interfacial area.[12] Here we apply the theories of Blumberg[24] and others[26,27,31] to calculate the time regime over which we should analyze the recovery curves for extracting this

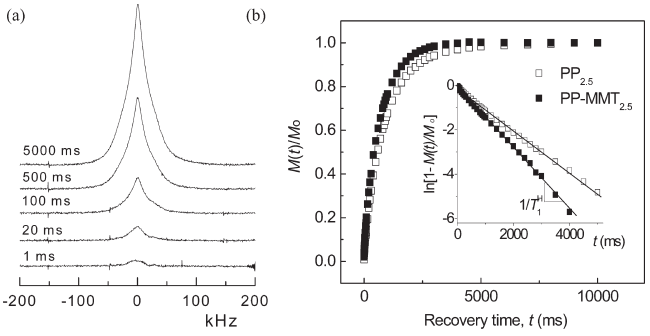

Figure 1. ^{1}H NMR magnetization recovery following saturation: (a) spectra, labeled with respective recovery time, for PP−MMT nanocomposite with stretch ratio λ = 2.5 (PP−MMT$_{2.5}$), and (b) normalized magnetization, $M(t)/M_0$, versus recovery time obtained by integrating ^{1}H spectra for PP−MMT$_{2.5}$ and the polypropylene with the same stretch ratio (PP$_{2.5}$). The inset in (b) displays the same data plotted as ln[1 − $M(t)/M_0$] vs recovery time, the slopes of which reflect the inverse T_1s. The nanocomposite exhibits faster relaxation (shorter T_1^{H}) than the corresponding polymer.

information. In other words, we want to apply eq 4, which describes the magnetization recovery in terms of N_p, so we would like an estimate of the time period, defined by eq 5, over which this equation is valid. For clays, N_p is analogous to the effective surface area and therefore should provide information on the degree of exfoliation.

To make this determination, we need estimates of the spin-diffusion barrier radius (δ), electron−nucleus coupling constant (C), and spin-diffusion coefficient (D). The barrier radius was estimated using the structure of the organically modified MMT (cf. Table 1) and some information obtained from its solid-state ^{13}C NMR spectrum. Figure 2 displays ^{13}C direct polarization MAS spectra of two organoclays: MMT, which contains paramagnetic species, and fluorohectorite, which is void of these impurities. Otherwise, FH is quite comparable to MMT. In particular, the packing densities and structures of the ammonium surfactant modifiers are similar for these two clays. The spectra were recorded under MAS and at 70 °C, above the transition to a liquidlike phase for dimethyldioctadecylammonium cations adsorbed onto mica surfaces,[39] to mitigate broadening due to residual dipolar couplings. The major peak at 30 ppm is due to conformationally disordered methylene chains, all-trans methylenes appear at 33 ppm, the chain-end methylene and methyl carbons appear at 23 and 15 ppm, respectively, and the ammonium head-group methylene and methyl carbons appear centered around 53 ppm. While all peaks are broader for MMT than for FH, the head-group carbons are broadened beyond detection. Thus, we propose that the head-group carbons are within the sphere of direct relaxation by the paramagnetic impurities in MMT. This observation was used to estimate the spin-diffusion barrier radius, δ, for our samples. The cross-sectional diameter of the head group is ~0.4 nm,[42] and the paramagnetic centers are located within clay platelets at a minimum distance of 0.5 nm from the nearest surface, leading to an estimate for the barrier radius of $\delta \leq 0.9$ nm. This estimate is consistent with ^{1}H NMR data on pure MMT (no organic modifier, 3.35 wt % Fe_2O_3), where[43] the absence of observable ^{1}H resonance peaks for surface hydroxyls indicates that δ is at least 0.5 nm. Our estimate is also consistent with a ^{29}Si NMR study on pure clay samples (0.1−5 wt % Fe_2O_3) in which the authors reported a δ of the order of 1 nm.[44]

VanderHart et al. measured ^{1}H Bloch decays at 300 MHz for commercial MMT and reported that 36% of the available protons were not detected.[33] We estimated that the spin-diffusion barrier radius extends about 0.4 nm into the gallery space from the surface of each platelet. The average gallery height for our

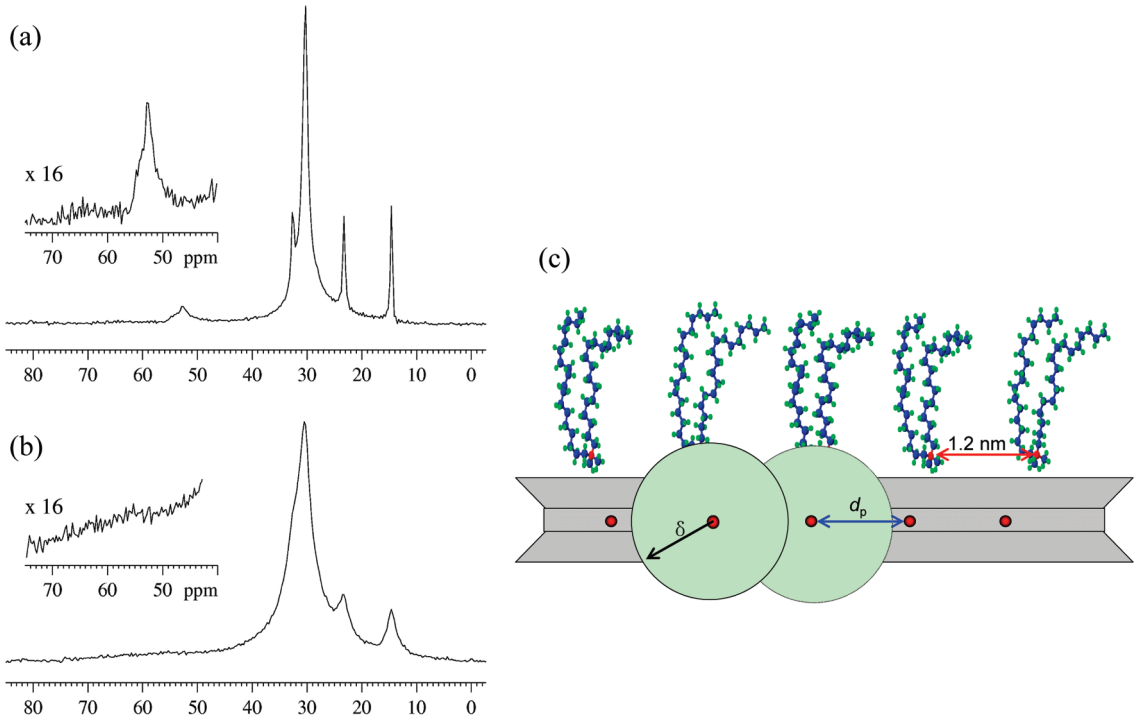

Figure 2. Solid-state ^{13}C direct polarization MAS spectra collected at 70 °C of organically modified (a) fluorohectorite and (b) montmorillonite which contains paramagnetic Fe^{3+} in the octahedral interlayer. The insets depict expanded regions for the methyl and methylene peaks of the ammonium head group. (c) Cartoon illustrating relative distances within an organically modified Cloisite 15A clay platelet. Paramagnetic Fe^{3+} centers are shown as spheres fixed in the middle plane and located on average $d_p = 1.2$ nm apart, estimated from N_p ($\sim 10^{21}$/cm^3) calculated from Fe^{3+} content and structural formula (see Table 1). Lateral packing of surface modifiers estimated at 1.2 nm from the area per cation assuming a cubic array. Surfactants are shown on only one surface of platelet as other surface may be stacked against other platelets. The spin-diffusion barrier radius δ is estimated to be 0.9 nm.

clay is 2.2 nm (basal spacing of 3.2 nm minus platelet thickness of 1 nm). Assuming a homogeneous distribution of ^{1}Hs in the gallery space, 0.8/2.2 = 36% of the ^{1}Hs in the galleries fall within the region $\leq \delta$ and should not be detectable, which is completely consistent with the data of VanderHart et al.[33]

The estimated spin-diffusion barrier radius δ gives us an idea of the extent to which direct relaxation by the paramagnetic centers reaches into the bulk sample from the center of the clay platelets. This is depicted in Figure 2c along with other relative distances within the organically modified MMT (i.e., Cloisite 15A) platelet. The magnitude of δ means that for stacked or layered platelets only the exposed outer surfaces play a role in shortening the nuclear T_1s in the organic matrix. The average separation between paramagnetic centers (d_p), estimated at 1.2 nm from the N_p ($\sim 10^{21}$/cm^3) which was calculated from the Fe^{3+} content and structural formula (see Table 1), is comparable in size to δ, thereby ensuring the entire exposed clay surface is rendered paramagnetic. Conceptually, the exposed clay surface is proportional to an effective number of paramagnetic centers, $N_{p,eff}$. With increasing exfoliation, $N_{p,eff}$ will increase.

The electron−nucleus coupling constant is given by eq 3. For a given sample, the only unknown is the electron spin−lattice correlation time, τ_c. We estimated this value for our clay from the measured ^{1}H spin−lattice relaxation time and structure of the organically modified clay (see Table 1). At 300 MHz, the average T_1 for the observable ^{1}Hs in Cloisite 15A is 10 ms. The observable ^{1}Hs are located 0.9−1.1 nm from a clay surface, with the lower boundary being the estimated spin-diffusion barrier and upper boundary calculated as half the distance to the neighboring clay surface: basal spacing, 3.2 nm, minus the platelet thickness, 1 nm, divided by 2. We assume that relaxation in these materials occurs primarily by direct interaction with the paramagnetic centers and is described by eq 2; thus, $1/T_1 = Cr^{-6}$. However, this equation is valid for interaction between a single electron and nucleus, and Figure 2c suggests that the nuclei nearer the surface can directly interact with multiple centers. Thus, we ignore the ^{1}Hs closest to the clay surface and consider the ones at 1.1 nm, which must have T_1s longer than the measured average of 10 ms. Using $r = 1.1$ nm and $T_1 > 10$ ms, we calculated a lower bound of $\tau_c > 10^{-9}$ s. This is consistent with T_1 data measured on the organically modified clay as a function of temperature (data not shown) at 300 MHz: With increasing temperature, T_1 decreases, indicating that $\omega_0\tau_c > 1$ and $\tau_c > 1/(2\pi \times 300\ \text{MHz}) > 5 \times 10^{-10}$ s. Our τ_c is also consistent with another reported τ_c estimate for commercial MMT.[33] Using $\tau_c > 10^{-9}$ s, we calculate the coupling constant using eq 3 to be $C < 2 \times 10^{-52}$ m^6/s.

The spin-diffusion coefficient for polypropylene has been reported to be as high as 0.5 nm^2/ms.[45,46] For estimating the time window for diffusion-limited relaxation, we used a D of 0.1 nm^2/ms, the room-temperature value for the D of amorphous polypropylene and polyethylene.[47,48] This smaller value was chosen to reflect the structure of the region immediately adjacent to the paramagnetic centers, in which surfactant tails are similar to polyethylene segments and conformationally disordered according to the ^{13}C solid-state NMR spectrum (see Figure 2). We also estimated the spin-diffusion coefficient from the ^{1}H line width of the organically modified FH, which is structurally analogous to the Cloisite 15A but without the line-broadening paramagnetic impurities, using an approach described by Hedesiu et al.[47] Since the line shape contained a rigid and amorphous component, two Ds were calculated and averaged[49] to obtain a single effective D of 0.1 nm^2/ms.

Using $\delta \sim 0.9$ nm, $C < 2 \times 10^{-52}$ m^6/s, and $D \sim 0.1$ nm^2/ms, we estimated the time window for diffusion-limited relaxation to be 3−14 ms (see eq 5). Figure 3a shows a plot of normalized and corrected magnetization, $[M(t)/M_0]_{PP\text{-}MMT} - [M(t)/M_0]_{PP}$, against the square root of recovery time for a series of PP−MMT nanocomposites with different stretch ratios. From 3 to 20 ms the

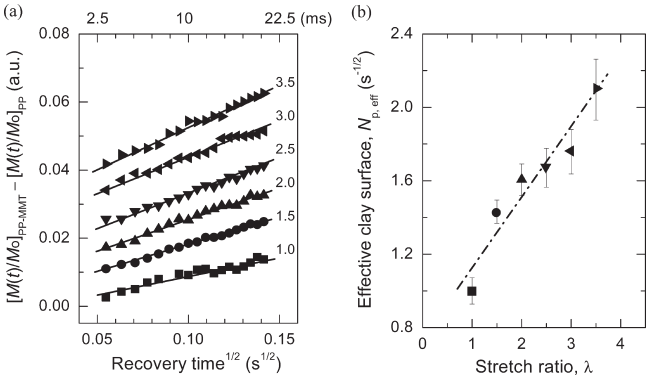

Figure 3. (a) Normalized and corrected magnetization, $[M(t)/M_0]_{PP-MMT} - [M(t)/M_0]_{PP}$, vs the square root of recovery time for PP−MMT nanocomposites with different stretch ratios (λ). PP−MMT and PP films were equibiaxially stretched at 16 s^{-1} and 150 °C. For a given λ, PP−MMT data were corrected using data from an identically deformed PP. Stretch ratios, from 1 (unstretched) to 3.5, are shown above the respective data for a given sample, which are vertically displaced to prevent overlap. Lines are linear least-square fits. Slopes of these lines, normalized to the slope of the line for $\lambda = 1$ and proportional to the exposed clay surface or effective number of paramagnetic centers $N_{p,eff}$, are plotted in (b) as a function of stretch ratio.

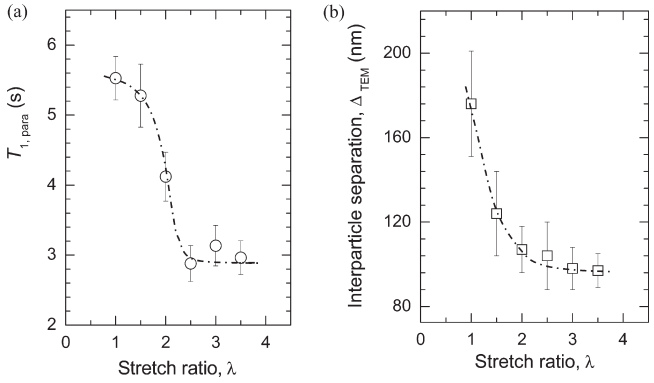

Figure 4. (a) Paramagnetic contribution to the overall NMR spin−lattice relaxation time, $T_{1,para}$ (from eq 9), and (b) average interparticle separation, Δ_{TEM}, from TEM data as functions of stretch ratio, λ, for PP−MMT films equibiaxially stretched at 16 s^{-1} and 150 °C. Unstretched sample has $\lambda = 1$. Dash-dotted lines are guides.

data can be fit well with straight lines ($R^2 > 0.99$), which is a strong indication of diffusion-limited relaxation. Above 20 ms, the data slowly deviate from linearity as the transition to exponential magnetization growth occurs. However, even up to 50 ms the data are reasonably linear with $\sqrt{t}$ ($R^2 = 0.95$). Data were also measured for recovery times below 3 ms, but they deviated significantly from the straight lines shown in Figure 3a. Thus, the lower boundary for diffusion-limited relaxation (cf. eq 5) was estimated quite precisely, while the upper boundary could be extended due to the gradual nature of the transition to exponential magnetization growth.

Crystallinity, although it increases slightly with stretch ratio, is identical for the PP and PP−MMT at a given stretch ratio.[10] The pure clay content was found by TGA to be 2.7% for all samples. Thus, differences in the normalized and corrected magnetization−recovery slopes of Figure 3 cannot be attributed to differences in polymer crystallinity or clay concentration. The slopes of the straight lines increase with increasing stretch ratio, which reflects the increase in the effective number of paramagnetic centers, $N_{p,eff}$, as new clay surface is exposed due to the shearing that occurs during the stretching process. The amount of new clay surface exposed for a given stretch ratio has been quantified by normalizing the slopes of Figure 3a by the slope for the sample that has not been stretched ($\lambda = 1$). This is shown in Figure 3b as clay surface vs stretch ratio. The amount of new clay surface exposed increases over 2-fold and is a near linear function of the equibiaxial stretch ratio up to $\lambda = 3.5$.

While the initial magnetization recovery provides information on the amount of exposed clay surface, the spin-diffusion-mediated long-time relaxation behavior provides information on the average interparticle spacing. As described by Bourbigot et al.,[12] the long-time relaxation behavior is quantitatively captured in the overall ^{1}H spin−lattice relaxation time of the nanocomposite, $T_{1,PCN}$. These values were measured and corrected for relaxation due to the pure polymer (cf. eq 9) to yield the paramagnetic contribution to the spin−lattice relaxation time, $T_{1,para}$, which is plotted in Figure 4a as a function of stretch ratio. In this plot, $T_{1,para}$ decreases at first slowly and then steeply from $\lambda = 1.5$ to $\lambda = 2.5$, after which an apparent plateau is reached. These data contrast the initial-slope data of Figure 3 which increase nearly linearly for all stretch ratios, signifying an increase in the amount of exposed clay surface for all stretch ratios. If the $T_{1,para}$ data simply reflected the amount of exposed clay surface, then they should decrease linearly as well. The $T_{1,para}$ data of Figure 4a indicate the average interparticle spacing decreases slowly at first, more rapidly up to $\lambda = 2.5$, and then levels off for higher stretch ratios. Decreasing $T_{1,para}$ values are characteristic of decreasing average interparticle separations since $T_{1,para}$ values are governed by the distances over which spin diffusion must occur to the paramagnetic relaxation sinks. These results are consistent with those obtained from TEM data. Average interparticle separations were measured by image analysis and are shown in Figure 4b as a function of stretch ratio. The TEM interparticle separations (Δ_{TEM}) decrease up to $\lambda = 2.5$, after which they plateau in agreement with the $T_{1,para}$ data. The slightly slower decrease from $\lambda = 1$ to 1.5 for the $T_{1,para}$ data are attributed to aggregate breakup without significant separation of the resulting daughter particles, which would not lead to a large decrease in $T_{1,para}$. The data are consistent with this explanation, especially considering the particle density increases rather significantly from 17 ± 4 at $\lambda = 1$ to 39 ± 7 at $\lambda = 1.5$. Average interparticle separations, particle densities, and other results obtained from analysis of TEM data are summarized in Table 2 and discussed below.

Table 2. Clay Morphology from TEM

stretch ratio, λ	interparticle separation, Δ_{TEM} (nm)[a]	particles/ μm^2	length (nm)[b]	thickness (nm)[c]
1	176 ± 25	17 ± 4	189 ± 86	6.4 ± 1.7
1.5	124 ± 20	39 ± 7	170 ± 70	5.8 ± 1.3
2	107 ± 11	45 ± 11	216 ± 95	4.9 ± 1.1
2.5	104 ± 16	41 ± 7	210 ± 84	4.5 ± 0.8
3	98 ± 10	40 ± 6	275 ± 126	3.1 ± 0.5
3.5	97 ± 8	30 ± 13	283 ± 191	2.0 ± 0.5

[a] Measured using method introduced by van Es.[50,51] [b] Two particles considered one when separated by < 2 nm in direction normal to platelet plane. [c] Single particle thickness determined as average of three positions along its length: middle and each of 2 ends.

Representative TEM images are shown in Figure 5 for each stretch ratio. The unstretched PP−MMT film contains nanoparticles that are reasonably well-dispersed and randomly oriented (cf. Figure 5a). Most of the clay exists in aggregates of 2−3 platelets while some single layers are found. Aggregates of stacked and skewed platelets exist; examples are marked with circles in the TEM image of Figure 5a. These aggregates are broken up, and the platelets are aligned with increasing stretch ratio. By $\lambda = 2-2.5$ (cf. Figure 5c,d), platelets are mostly aligned, but the existence of some thick particles suggests that further exfoliation can take place with increasing stretch ratio, which is

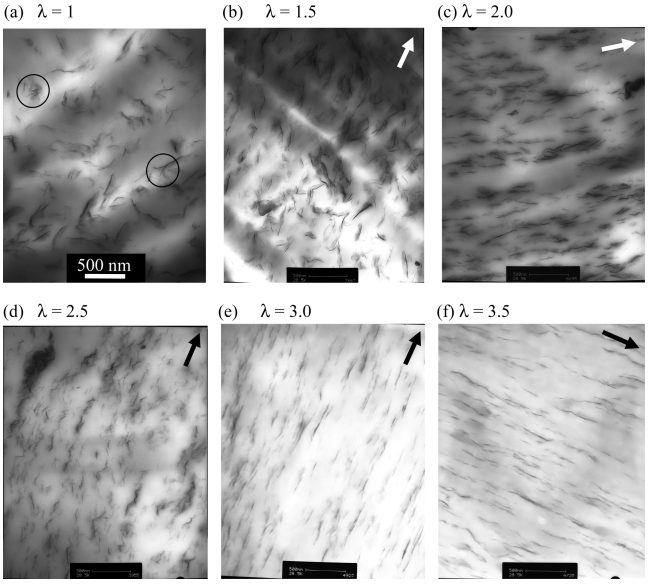

Figure 5. Representative TEM images of PP−MMT films with stretch ratios from $\lambda = 1$ (unstretched) (a) to $\lambda = 3.5$ (f). Samples were equibiaxially stretched at 150 °C and 16 s^{-1}. Scale shown in (a), 500 nm, is the same for each image. Circles shown in (a) mark the presence of stacked and skewed clay platelets. Arrows indicate the primary direction of orientation of clay particles. Sections for TEM were sliced along the direction normal to the film surface and therefore normal to the stretch direction.

consistent with the NMR data of Figures 3 and 4. Shearing of aligned clay particles leads to further exfoliation for stretch ratios of 3 and 3.5 (cf. Figures 3 and 5e,f).

A single orientation direction, marked with arrows, is evident in the micrographs of Figure 5. The nanocomposite sheets were stretched biaxially in the $x-y$ plane while the TEM images are views of either $x-z$ or $y-z$ cross sections. The appearance of single primary orientation directions for the clay particles, which are essentially disks, indicates the particles orient parallel to the $x-y$ plane of the sheet. TEM projections in the $x-y$ plane would more clearly illustrate the effect of biaxial stretching on clay particle orientation; however, microtoming samples in this plane is very difficult as the sheets are so thin.

Quantitative image analysis of the TEM data provided a wealth of information that is summarized in Table 2. With increasing stretch ratio, interparticle separation (Δ_{TEM}) is decreased, particle length increases, and particle thickness decreases. The particle density increases significantly for $\lambda = 1.5$ and then remains mostly constant, given the error ranges, for higher stretch ratios. These findings are consistent with shear-induced disintegration and exfoliation of clay aggregates. Wide-angle X-ray diffraction (WAXD) data (not shown) reveal the d_{001} basal spacing for the organically modified MMT expands from 3.19 to 3.27 nm in the unstretched PP−MMT nanocomposite, suggesting that some PP chains have intercalated into the clay galleries. These chain segments can effectively transfer stress to the platelets, weaken interplatelet interactions, and thereby facilitate separation and exfoliation.[5,6]

The TEM and WAXD data can be used to extract more information from the NMR data. The initial-slope data of Figure 3 showed that the exposed clay surface more than doubled when the unstretched film was equibiaxially stretched to $\lambda = 3.5$. This relative change can be converted into absolute information by estimating the average number of platelets per particle in the unstretched PP−MMT from the average particle thickness of 6.4 ± 1.7 nm (see Table 2). From WAXD data, we know the interplatelet spacing is 3.27 nm. Since this value reflects the mid-platelet to mid-platelet spacing, and a platelet is 1 nm thick, the

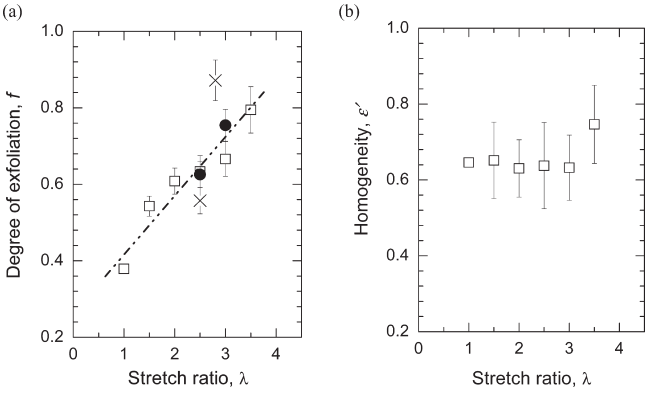

Figure 6. Degree of exfoliation, f (a), and homogeneity, ε', of clay dispersion (b) as a function of stretch ratio, λ, for PP−MMT films. Samples were equibiaxially stretched at 150 °C and 16 s^{-1} (□), 150 °C and 32 s^{-1} (●), or 145 °C and 16 s^{-1} (×). Unstretched sample has $\lambda = 1$.

corresponding thickness for a 2-platelet stack in a TEM image is taken to be 4.27 nm. Similarly, a 3-platelet stack should be 7.54 nm. Thus, the average particle in the unstretched PP−MMT contains between 2 and 3 platelets; interpolating between 4.27 and 7.54 nm yields an average number of platelets per particle of 2.64. We can now calculate a degree of exfoliation, f, using eq 8 since $N_{p,eff} = S/S_{ref}$ and the number of platelets/stack is 2.64 for the reference material: $f = N_{p,eff}/2.64$. Results are summarized in Table 3 and plotted in Figure 6a as a function of stretch ratio. The degree of exfoliation increases roughly linearly from 0.38 at $\lambda = 1$ to 0.8 at $\lambda = 3.5$. From TEM, the average particle thickness at $\lambda = 3.5$ is 2.0 ± 0.5 nm, which means that the average clay particle is between 1 and 2 platelets thick, that is, between 1 and 4.27 nm thick. Interpolating as before, the average number of platelets/stack at $\lambda = 3.5$ is 1.3, so the degree of exfoliation determined from TEM data alone is 0.77 (see eq 8), entirely consistent with the 0.8 value determined from NMR. After equibiaxial stretching to $\lambda = 3.5$, the PP−MMT nanocomposite maintains some potential for further exfoliation: The degree of exfoliation has not yet leveled off in the plot of f vs λ (see Figure 6a).

The degree of exfoliation was used to scale the idealized interparticle separation of 103 nm calculated from the clay and polymer volume fractions using eq 7 (2.7 wt % clay, 2.6 g/cm^3 MMT, 0.91 g/cm^3 PP). The scaled ideal interparticle separations were calculated as Δ_{ideal}/f and are summarized in Table 3. These Δ_{ideal}/f values, which obviously decrease with increasing exfoliation, were calculated using the definition of Bourbigot et al.[12] They used these values to determine a homogeneity index by comparing them with apparent interparticle spacings (cf. eq 10) that they extracted from modeling the long-time behavior of magnetization−recovery curves. Here we calculate a slightly different homogeneity index, ε'. We use the same ideal interparticle spacing scaled by the NMR-determined degree of exfoliation (Δ_{ideal}/f), but instead of an NMR-determined apparent interparticle spacing, we compare Δ_{ideal}/f with the interparticle spacings determined from TEM (Δ_{TEM}):

$$\varepsilon' = \Delta_{TEM}/(\Delta_{ideal}/f) \tag{11}$$

Homogeneity values were calculated for the PP−MMT samples using eq 11 and are listed in Table 3 and plotted in Figure 6b as a function of stretch ratio. The ε' values are constant from $\lambda = 1$ to $\lambda = 3$ but then increase slightly for $\lambda = 3.5$ as the degree of exfoliation jumps from 0.67 to 0.8 at this stretch ratio. Thus, homogeneity of the unstretched sample is not affected by stretching until higher strain levels are reached. It is interesting to note that the Δ_{TEM} values are nearly identical to the calculated Δ_{ideal} of 103 nm from $\lambda = 2$ to $\lambda = 3.5$ (see Table 2 and Figure 4b), but the

homogeneity increases slightly from $\lambda = 3$ to $\lambda = 3.5$. Calculation of the ideal interparticle separation from component volume fractions only accounts for the height or thickness of a single clay platelet, not its lateral dimensions (cf. eq 7). Finite lateral dimensions should result in reduced actual interparticle separations, while aggregation should increase actual interparticle separations. The increase in homogeneity from $\lambda = 3$ to $\lambda = 3.5$ is attributed to the increase in exfoliation due to sliding platelets apart that results in an increase in lateral particle dimensions.

The PP−MMT nanocomposites described thus far were equibiaxially stretched at 150 °C and 16 s^{-1}. The effect of strain rate was examined by stretching two samples at 32 s^{-1} (and 150 °C) to stretch ratios of $\lambda = 2.5$ and $\lambda = 3$. The degrees of exfoliation for these two samples are included in Figure 6a and reveal that doubling the shear rate at this deformation temperature does not significantly affect the clay morphology. On the other hand, a small decrease in the deformation temperature to 145 °C does have a significant effect. Two samples were stretched at 145 °C (and 16 s^{-1}) to stretch ratios of $\lambda = 2.5$ and $\lambda = 2.8$. The degrees of exfoliation for these two samples are also included in Figure 6a: The PP−MMT stretched to $\lambda = 2.8$ exhibits the highest exfoliation degree ($f = 0.87$) of all the samples in this study. We attribute this result to a higher melt viscosity at 145 °C, which leads to more effective stress transfer from polymer to clay particles. Indeed, onset of melting for these nanocomposites was observed by DSC at around 150 °C. Higher melt viscosities and larger shear stresses have been shown to facilitate exfoliation.[4,52] Thus, although the strain rate has seemingly little effect on exfoliation at 150 °C, we expect the strain rate will affect results more significantly at lower temperatures, where the transfer of shear stress from polymer to clay is improved.

A schematic depicting the evolution of clay morphology upon equibiaxial stretching PP−MMT nanocomposites is shown in Figure 7. This schematic summarizes the major findings from the NMR and TEM data. New clay surface is exposed throughout the stretching process (see Figures 3b and 6a), initially by breakup of large and skewed aggregates and lastly by sliding of platelets apart from each other. The average particle thickness decreases and the length increases (see Table 2), while the interparticle separation decreases to a plateau for the higher stretch ratios as the particles are aligned (see Figure 4).

With the exception of elastic modulus, the mechanical properties reported by Abu-Zurayk et al.[10] were shown to be diminished in the unstretched and low stretch ratio PP−MMT sheets but improved in a linear manner as stretch ratio increased. The reduction in yield and break stress is attributed to the presence of large clay tactoids which act as stress concentrators and initiate failure at large strains (but would not detrimentally influence low-strain properties such as elastic modulus). As the stretch ratio increases, it has been shown that the degree of exfoliation increases in a near linear manner (Figure 6) as the clay stacks are exfoliated, and this reduction in tactoid size is reflected in a linear increase in yield and break stress. The elastic modulus of the PP−MMT sheet was unchanged relative to the pure PP in the unstretched sheet and at low stretch ratios. Modulus enhancement was not evident until a stretch ratio of 2.5 was achieved after which modulus increased linearly with increasing stretch ratio. This is the ratio at which there is a large change in clay particle alignment from random to oriented as shown in Figure 4 where the interparticle separation reaches a plateau region. After this point the stretch ratio begins to have an influence on modulus such that modulus increases linearly with increasing degree of exfoliation (it should be noted that the changes in mechanical properties upon the addition of clay were shown not to be a consequence of changes in crystallinity).[10]

We calculated a degree of exfoliation (f) from NMR data using a reference sample for which the number of platelets per stack was estimated from an average particle thickness measured by TEM. The f value at $\lambda = 3.5$ is ~0.8 whether it is calculated from the TEM-scaled NMR data or from the TEM data alone. Degrees of exfoliation were also computed for the other four samples ($\lambda =$ 1.5, 2, 2.5, and 3) from their TEM-determined average particle thicknesses (cf. Table 2). The value for the sample at $\lambda = 3$ is 0.61, sufficiently similar to 0.67 computed from NMR data (cf. Table 3). However, the values for the remaining three samples ($\lambda = 1.5$, 2, and 2.5) are all lower by a factor of 3/4 from the ones determined from NMR data. We attribute this difference to the nature of the data collected using two separate techniques and the assumptions we used to determine the average number of platelets per stack. The TEM data provide distributions of particle thicknesses from which an average is calculated. This average is then placed discretely between two possible platelet stacks

Table 3. Clay Morphology from NMR

stretch ratio, λ	effective clay surface, $N_{p,eff}$	degree of exfoliation,[a] f	Δ_{ideal}/f (nm)[b]	homogeneity,[c] ε'
1	1	0.38	273	0.65
1.5	1.43 ± 0.07	0.54 ± 0.03	190 ± 5	0.65 ± 0.10
2	1.61 ± 0.09	0.61 ± 0.04	170 ± 6	0.63 ± 0.07
2.5	1.67 ± 0.11	0.63 ± 0.05	163 ± 7	0.64 ± 0.11
3	1.76 ± 0.12	0.67 ± 0.05	155 ± 7	0.63 ± 0.09
3.5	2.10 ± 0.16	0.80 ± 0.06	130 ± 8	0.75 ± 0.10

[a] $f = N_{p,eff}/2.64$, where 2.64 is platelets/stack in unstretched sample (i.e., reference material). [b] Scaled ideal interparticle separation where $\Delta_{ideal} = 103$ nm (see eq 7).[12] [c] $\varepsilon' = \Delta_{TEM}/(\Delta_{ideal}/f)$.

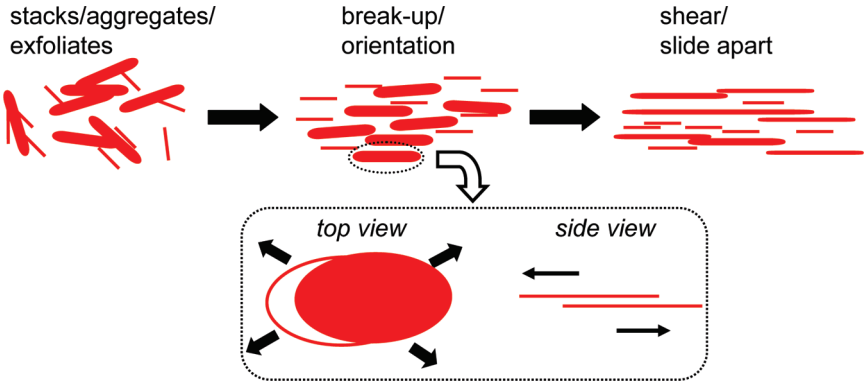

Figure 7. Schematic depicting the evolution of clay morphology under the action of equibiaxial stretching of PP−MMT nanocomposites. According to NMR data, new clay surface emerges for all stretch ratios up to $\lambda = 3.5$. For stretch ratios $\lambda < 2.5$, large aggregates are broken up and oriented. At larger stretch ratios $\lambda \geq 2.5$, particles are highly oriented and new clay surface emerges by sliding platelets apart, lengthening, and thinning the clay particles. This latter process is illustrated at the bottom of the schematic by the top and side views of an oriented stack.

(e.g., 2-platelet and 3-platelet), and then interpolation leads to an average number of platelets per stack. Thus, we essentially throw out the actual distribution and replace it with a distribution consisting of two stacks. The NMR method directly provides the change in the total effective clay surface, $N_{p,eff}$. Consideration of particle distributions is unnecessary when quantifying the relative differences seen in Figure 3b. To convert the NMR-determined $N_{p,eff}$ values to degrees of exfoliation, a reference material must be selected; given the assumptions involved in determining the average number of platelets/stack from TEM data, the best reference sample is probably one that is fully exfoliated.[12] The real advantage to using NMR and TEM in the integrated manner described in this report is that it eliminates the need for conducting labor-intensive TEM on all samples.

According to eq 5, the time window for diffusion-limited relaxation can be expanded by increasing the electron−nucleus coupling constant. Examination of eq 3 reveals that this is easily accomplished by simply making measurements at lower magnetic fields (ω_n in eq 3). We tested this by conducting saturation−recovery experiments on a bench-top NMR spectrometer operating at 23 MHz and discovered that the portion of the magnetization recovery curve that is linear with $\sqrt{t}$ did indeed increase by a factor of ~2. As low-field bench-top NMR spectrometers are common in industrial environments, this NMR methodology may have applications for process control and development.

Conclusions

Nanocomposites of polypropylene (PP) and 5 wt % organically modified montmorillonite (MMT), which contains ~3.5 wt % Fe^{3+} based on the pure clay, exhibit solid-state ^1H saturation recovery curves that are exponential for long times but linear with $\sqrt{t}$ for very short times (≤~20 ms). The $\sqrt{t}$ dependence for the short-time portions of these magnetization recovery curves is indicative of diffusion-limited relaxation. Considering the structure and NMR properties of the MMT, estimates of the spin-diffusion barrier radius (0.9 nm), electron−nucleus coupling constant ($< 2 \times 10^{-52}$ m^6/s), and spin-diffusion coefficient (0.1 nm^2/ms) were used to calculate the time window for diffusion-limited relaxation as 3−14 ms. Thus, the initial slopes of these relaxation curves were directly proportional to the number of paramagnetic centers, effectively a measure of the exposed clay surface, or degree of exfoliation. Spin−lattice relaxation times, determined from the entire relaxation curves, could be corrected to yield the paramagnetic contribution to the overall relaxation time ($T_{1,para}$), which provided information on the average interparticle separation.

The PP−MMT nanocomposites were equibiaxially stretched at 150 °C and 16 s^{-1}. The exposed clay surface increased with stretch ratio up to $\lambda = 3.5$ while the interparticle separation decreased until reaching a plateau at $\lambda \sim 2.5$. These NMR data were consistent with TEM images which revealed the particle thickness decreased continuously with stretch ratio up to $\lambda = 3.5$, while the interparticle separation decreased until reaching a plateau for $\lambda > 2$. TEM also revealed the average particle length increased with increasing stretch ratio, but most significantly for the largest strains ($\lambda \geq 3$). Evolution of clay morphology proceeds by aggregate breakup and orientation at lower strains followed by sliding aligned platelets apart at higher strains. Stretching at a slightly lower temperature of 145 °C led to a higher degree of exfoliation at $\lambda = 2.8$ but not at $\lambda = 2.5$ when compared to the samples stretched at 150 °C to the same or similar stretch ratios. We attribute this to more effective shear transfer in higher viscosities.

The TEM and NMR data were integrated to yield quantitative morphology descriptors for degree of exfoliation and homogeneity. The degree of exfoliation increased from 0.38 to 0.8 upon equibiaxial stretching to $\lambda = 3.5$, while the homogeneity was constant around 0.65 up to $\lambda = 3$ and increased slightly to 0.75 at $\lambda = 3.5$. The degree of exfoliation (f) is defined exactly as Bourbigot et al.[12] have defined it; although we used a different reference, full exfoliation still means $f = 1$. The homogeneity, defined differently from Bourbigot et al.,[12] is simply a measure of how TEM interparticle separations compare with f-scaled interparticle separations calculated from component volume fractions for an "ideal" nanocomposite in which the clay is fully exfoliated and perfectly layered. In addition to interparticle separations, calculated homogeneity values reflect finite particle lengths.

Acknowledgment. Funding for this work was granted by the National Science Foundation (DMR-0710501) in the US and by the Engineering and Physical Sciences Research Council in the UK. The authors express their sincere thanks to Southern Clay products for providing Cloisite 15A and supporting data and to one of the reviewers (DVH) for very helpful comments and suggestions.

References and Notes

(1) Chen, B.; Evans, J. R. G.; Greenwell, H. C.; Boulet, P.; Coveney, P. V.; Bowden, A. A.; Whiting, A. *Chem. Soc. Rev.* **2008**, *37* (3), 568–594.
(2) Finnigan, B.; Jack, K.; Campbell, K.; Halley, P.; Truss, R.; Casey, P.; Cookson, D.; King, S.; Martin, D. *Macromolecules* **2005**, *38* (17), 7386−7396.
(3) Kim, D. H.; Fasulo, P. D.; Rodgers, W. R.; Paul, D. R. *Polymer* **2007**, *48*, 5960–5978.
(4) Vermogen, A.; Masenelli-Verlot, K.; Séguéla, R.; Duchet-Rumeau, J.; Boucard, S.; Prele, P. *Macromolecules* **2005**, *38* (23), 9661–9669.
(5) Zhang, Q.; Wang, Y.; Fu, Q. *J. Polym. Sci., Part B: Polym. Phys.* **2003**, *41* (1), 1–10.
(6) Dennis, H. R.; Hunter, D. L.; Chang, D.; Kim, S.; White, J. L.; Cho, J. W.; Paul, D. R. *Polymer* **2001**, *42* (23), 9513–9522.
(7) Okamoto, M.; Nam, P. H.; Maiti, P.; Kotaka, T.; Nakayama, T.; Takada, M.; Ohshima, M.; Usuki, A.; Hasegawa, N.; Okamoto, H. *Nano Lett.* **2001**, *1* (9), 503–505.
(8) Cole, K. C.; Perrin-Sarazin, F.; Dorval-Douville, G. *Macromol. Symp.* **2005**, *230*, 1–10.
(9) Rajiv, R. S.; Harkin-Jones, E.; Soon, K.; McNally, T.; Menary, G.; Armstrong, C. G.; Martin, P. J. *Eur. Polym. J.* **2009**, *45*, 332–340.
(10) Abu-Zurayk, R.; Harkin-Jones, E.; McNally, T.; Menary, G.; Martin, P.; Armstrong, C. *Compos. Sci. Technol.* **2009**, *69*, 1644–1652.
(11) Eckel, D. F.; Balogh, M. P.; Fasulo, P. D.; Rodgers, W. R. *J. Appl. Polym. Sci.* **2004**, *93*, 1110–1117.
(12) Bourbigot, S.; VanderHart, D. L.; Gilman, J. W.; Awad, W. H.; Davis, R. D.; Morgan, A. B.; Wilkie, C. A. *J. Polym. Sci., Part B: Polym. Phys.* **2003**, *41* (24), 3188–3213.
(13) Vaia, R. A. Structural Characterization of Polymer-Layered Silicate Nanocomposites. In *Polymer-Clay Nanocomposites*; Pinnavaia, T. J., Beal, G. W., Eds.; John Wiley & Sons: New York, 2000; pp 229−266.
(14) Vaia, R. A.; Liu, W. *J. Polym. Sci., Part B: Polym. Phys.* **2002**, *40*, 1590–1600.
(15) Monticelli, O.; Musina, Z.; Russo, S.; Bals, S. *Mater. Lett.* **2007**, *61*, 3446–3450.
(16) Morgan, A. B.; Gilman, J. W. *J. Appl. Polym. Sci.* **2003**, *87* (8), 1329–1338.
(17) Samyn, F.; Bourbigot, S.; Jama, C.; Bellayer, S.; Nazare, S.; Hull, R.; Castrovinci, A.; Fina, A.; Camino, G. *Eur. Polym. J.* **2008**, *44*, 1642–1653.
(18) Okamoto, M.; Nam, P. H.; Maiti, P.; Kotaka, T.; Hasegawa, N.; Usuki, A. *Nano Lett.* **2001**, *1* (6), 295–298.
(19) Wang, K.; Liang, S.; Deng, J. N.; Yang, H.; Zhang, Q.; Fu, Q.; Dong, X.; Wang, D. J.; Han, C. C. *Polymer* **2006**, *47* (20), 7131–7144.
(20) Wang, K.; Zhao, P.; Yang, H.; Liang, S.; Zhang, Q.; Du, R. N.; Fu, Q. A.; Yu, Z. Q.; Chen, E. Q. *Polymer* **2006**, *47* (20), 7103–7110.
(21) Perrin-Sarazin, F.; Ton-That, M.-T.; Bureau, M. N.; Denault, J. *Polymer* **2005**, *46*, 11624–11634.

(22) Preschilla, N.; Sivalingam, G.; Abdul Rasheed, A. S.; Tyagi, S.; Biswas, A.; Bellare, J. R. *Polymer* **2008**, *49*, 4285–4297.
(23) Bloembergen, N. *Physica* **1949**, *15* (3−4), 386–426.
(24) Blumberg, W. E. *Phys. Rev.* **1960**, *119* (1), 79–84.
(25) Abragam, A. *Principles of Nuclear Magnetism*; Clarendon Press: Oxford, 1961; p 599.
(26) Rorschach, H. E. *Physica* **1964**, *30* (1), 38–48.
(27) Lowe, I. J.; Tse, D. *Phys. Rev.* **1968**, *166* (2), 279–291.
(28) Tse, D.; Lowe, I. J. *Phys. Rev.* **1968**, *166* (2), 292–302.
(29) Tse, D.; Hartmann, S. R. *Phys. Rev. Lett.* **1968**, *21* (8), 511–514.
(30) Degennes, P. G. *J. Phys. Chem. Solids* **1958**, *7* (4), 345–350.
(31) Gosele, U. *Physica B+C* **1976**, *85* (2), 317–322.
(32) VanderHart, D. L.; Asano, A.; Gilman, J. W. *Macromolecules* **2001**, *34* (12), 3819–3822.
(33) VanderHart, D. L.; Asano, A.; Gilman, J. W. *Chem. Mater.* **2001**, *13* (10), 3781–3795.
(34) VanderHart, D. L.; Asano, A.; Gilman, J. W. *Chem. Mater.* **2001**, *13* (10), 3796–3809.
(35) McNally, T.; Murphy, W. R.; Lew, C. Y.; Turner, R. J.; Brennan, G. P. *Polymer* **2003**, *44* (9), 2761–2772.
(36) Xie, W.; Xie, R.; Pan, W.-P.; Hunter, D.; Koene, B.; Tan, L.-S.; Vaia, R. *Chem. Mater.* **2002**, *14* (11), 4837–4845.
(37) Yang, J. H.; Han, Y. S.; Choy, J. H.; Tateyama, H. *J. Mater. Chem.* **2001**, *11* (4), 1305–1312.
(38) Schmidt, D. F.; Clement, F.; Giannelis, E. P. *Adv. Funct. Mater.* **2006**, *16* (3), 417–425.
(39) Osman, M. A.; Ernst, M.; Meier, B. H.; Suter, U. W. *J. Phys. Chem. B* **2002**, *106* (3), 653–662.
(40) Blum, A. E.; Eberl, D. D. *Clays Clay Miner.* **2004**, *52* (5), 589–602.
(41) Martin, P. J.; Tan, C. W.; Tshai, K. Y.; McCool, R.; Menary, G.; Armstrong, C. G.; Harkin-Jones, E. *Plast. Rubber Compos.* **2005**, *34* (5/6), 276–282.
(42) Okuyama, K.; Soboi, Y.; Iijima, N.; Hirabayashi, K.; Kunitake, T.; Kajiyama, T. *Bull. Chem. Soc. Jpn.* **1988**, *61* (5), 1485–1490.
(43) Levin, E. M.; Hou, S. S.; Bud'ko, S. L.; Schmidt-Rohr, K. *J. Appl. Phys.* **2004**, *96* (9), 5085–5092.
(44) Labouriau, A.; Kim, Y. W.; Earl, W. L. *Phys. Rev. B* **1996**, *54* (14), 9952–9959.
(45) Quijada-Garrido, I.; Wilhelm, M.; Spiess, H. W.; Barrales-Rienda, J. M. *Macromol. Chem. Phys.* **1998**, *199*, 985–995.
(46) Chen, Q.; Schmidt-Rohr, K. *Solid State Nucl. Magn. Reson.* **2005**, *29*, 142–152.
(47) Hedesiu, C.; Demco, D. E.; Kleppinger, R.; Vanden Poel, G.; Gijsbers, W.; Blumich, B.; Remerie, K.; Litvinov, V. M. *Macromolecules* **2007**, *40* (11), 3977–3989.
(48) Hedesiu, C.; Demco, D. E.; Kleppinger, R.; Buda, A. A.; Blumich, B.; Remerie, K.; Litvinov, V. M. *Polymer* **2007**, *48* (3), 763–777.
(49) Mellinger, F.; Wilhelm, M.; Spiess, H. W. *Macromolecules* **1999**, *32* (14), 4686–4691.
(50) van Es, M. Polymer-Clay Nanocomposites: The Importance of Particle Dimensions Technische Universiteit Delft, 2001.
(51) Bertmer, M.; Wang, M. F.; Kruger, M.; Blumich, B.; Litvinov, V. M.; van Es, M. *Chem. Mater.* **2007**, *19* (5), 1089–1097.
(52) Fornes, T. D.; Yoon, P. J.; Keskkula, H.; Paul, D. R. *Polymer* **2001**, *42* (25), 9929–9940.